

Star formation and figure rotation in the early-type galaxy NGC 2974

Hyunjin Jeong,^{1,2*} Martin Bureau,² Sukyoung K. Yi,^{1,2} Davor Krajnović², and Roger L. Davies²

¹*Department of Astronomy, Yonsei University, Seoul 120-749, Korea*

²*Sub-Department of Astrophysics, University of Oxford, Denys Wilkinson Building, Keble Road, Oxford OX1 3RH*

30 June 2018

ABSTRACT

We present *Galaxy Evolution Explorer* (*GALEX*) far (FUV) and near (NUV) ultraviolet imaging of the nearby early-type galaxy NGC 2974, along with complementary ground-based optical imaging. In the ultraviolet, the galaxy reveals a central spheroid-like component and a newly discovered complete outer ring of radius 6.2 kpc, with suggestions of another partial ring at an even larger radius. Blue FUV–NUV and UV–optical colours are observed in the centre of the galaxy and from the outer ring outward, suggesting young stellar populations ($\lesssim 1$ Gyr) and recent star formation in both locations. This is supported by a simple stellar population model which assumes two bursts of star formation, allowing us to constrain the age, mass fraction and surface mass density of the young component pixel by pixel. Overall, the mass fraction of the young component appears to be just under 1 per cent (lower limit, uncorrected for dust extinction). The additional presence of a nuclear and an inner ring (radii 1.4 and 2.9 kpc, respectively), as traced by [O III] emission, suggests ring formation through resonances. All three rings are consistent with a single pattern speed of 78 ± 6 km s⁻¹ kpc⁻¹, typical of S0 galaxies and only marginally slower than expected for a fast bar if traced by a small observed surface brightness plateau. This thus suggests that star formation and morphological evolution in NGC 2974 at the present epoch are primarily driven by a rotating asymmetry (probably a large-scale bar), despite the standard classification of NGC 2974 as an E4 elliptical.

Key words: galaxies: elliptical and lenticular, cD – galaxies: evolution – galaxies: individual: NGC 2974 – galaxies: photometry – galaxies: structure – ultraviolet: galaxies.

1 INTRODUCTION

Early-type galaxies are traditionally viewed as dynamically simple stellar systems with homogeneous stellar populations (e.g. Gott 1977). However, building on earlier work (e.g. de Zeeuw & Franx 1991 and references therein), the SAURON survey (Bacon et al. 2001; de Zeeuw et al. 2002) of the two-dimensional ionised-gas/stellar kinematics and stellar populations of nearby early-type galaxies has recently revealed kinematically-decoupled components and substantial metallicity and/or age gradients in many objects (e.g. Emsellem et al. 2004; Sarzi et al. 2006; Kuntschner et al. 2006). Early-type galaxies are thus likely to have had complex and varied formation histories. Such properties are often taken as evidence against the classical monolithic collapse model (e.g. Eggen, Lynden-Bell & Sandage 1962;

Larson 1974), in which elliptical galaxies are old systems that formed early in highly efficient starbursts and have evolved passively since.

Indeed, while standard optical imaging shows that most early-type galaxies have red colours and old stellar populations, deep imaging surveys have shown that many possess shells and tidal features (e.g. Schweizer & Seitzer 1992), tell-tale signs of a turbulent past. Colour gradients also indicate that early-type galaxies have composite stellar populations (e.g. Peletier et al. 1990), and some nearby early-type galaxies have signatures of ongoing or recent star formation (RSF; e.g. NGC 2865; Hau, Carter & Balcells 1999; Raimann et al. 2005). Spectroscopic studies further suggest that many elliptical galaxies have intermediate-age stars (e.g. O’Connell 1980; Bica & Alloin 1987; Trager et al. 2000). The spread in the luminosity-weighted age (e.g. Trager et al. 2000) is evidence for RSF. The so-called E + A galaxies (Dressler & Gunn 1983) possess characteristic spec-

* E-mail: hyunjin@galaxy.yonsei.ac.kr

tral features defined by strong hydrogen Balmer absorption lines ($H\delta$, $H\gamma$, $H\beta$), indicating the presence of a young stellar population, but have negligible $[O II] \lambda 3727$ emission. These galaxies are believed to be ‘post-starburst’ systems, i.e. they have recently undergone a burst of star formation. Fukugita et al. (2004) also suggested that a small fraction of low redshift elliptical galaxies have unambiguous signatures of active star formation with rates as high as those in spirals.

Far ultraviolet (FUV) radiation was first discovered in early-type galaxies by the *Orbiting Astronomical Observatory-2* in 1969 (Code, Welch & Page 1972), but it is now generally recognized that UV emission is a ubiquitous phenomenon in these objects. Although star formation (SF) can also be measured indirectly at other wavelengths, particularly in the infrared (e.g. Hunter et al. 1986; Meurer et al. 1997) and through $H\alpha$ emission (e.g. Kennicutt 1983; Hirashita, Buat & Inoue 2003), UV light is very sensitive to stellar populations younger than a few hundred megayears and the UV flux can give important and direct information about the star formation rate (e.g. Hirashita et al. 2003; Burgarella, Buat & Iglesias-Páramo 2005). The FUV is sensitive to the UV upturn flux originating from old hot helium-burning horizontal branch (HB) stars (see, e.g., Yi, Demarque & Oemler 1997 and O’Connell 1999 for reviews of this issue and the UV upturn phenomenon), hence SF studies usually focus on the near ultraviolet (NUV) passband. Ferreras & Silk (2000) studied young stars in the cluster Abell 851 ($z = 0.41$) using NUV–optical colours and suggested that, for some of the early-type galaxies, the stellar mass fraction in young stars is higher than 10 per cent. More recently, Yi et al. (2005) investigated the NUV colour–magnitude relation of early-type galaxies classified by the Sloan Digital Sky Survey. They concluded that roughly 15 per cent of nearby bright ($M_r < -22$) early-type galaxies show signs of recent ($\lesssim 1$ Gyr) star formation (at the 1–2 per cent level by stellar mass).

Here, we focus on the nearby early-type galaxy NGC 2974, classified as E4 in the RC3 (de Vaucouleurs et al. 1991) but possessing many features (mainly dynamical) more reminiscent of lenticular galaxies (see, e.g., Cinzano & van der Marel 1994). NGC 2974 has in fact been widely studied because of its unusual physical properties, including a dust lane containing ionised gas (e.g. Kim 1989) and substantial neutral hydrogen (HI) consistent with a rotating disc aligned with the optical isophotes (e.g. Kim et al. 1988). Buson et al. (1993) also suggested that it has a complex lens-like feature. Recently, using data from the TIGER integral-field spectrograph and *Hubble Space Telescope’s* (*HST*) Wide Field and Planetary Camera 2 (WFPC2), Emsellem, Goudfrooij & Ferruit (2003) discovered a gaseous two-arm spiral structure in the central 500 pc, suggesting the presence of a nuclear bar. The larger scale SAURON integral-field observations of Krajnović et al. (2005) reveal an apparent nuclear bar, nuclear ring, larger scale spiral arms and a possible inner ring in the ionised gas map (see Section 4.1), which suggest the presence of a large-scale bar as well.

In this paper, we present and discuss new UV imaging observations of NGC 2974 obtained with *Galaxy Evolution Explorer* (*GALEX*). In Section 2, we describe the *GALEX* observations and data reduction, supporting optical imag-

ing, and the main results from UV–optical surface photometry. Recent star formation in NGC 2974 is quantified and discussed in Section 3, and evidence for a rotating pattern, mainly based on the discovery of a star-forming outer ring, is discussed in Section 4. We summarize our results and discuss their implications briefly in Section 5.

2 OBSERVATIONS AND MAIN RESULTS

2.1 UV observations and data analysis

We observed NGC 2974 with the Medium imaging mode of *GALEX* on 2005 February 19, part of a larger survey of the galaxy sample from the SAURON project (see de Zeeuw et al. 2002). A NASA small explorer mission, *GALEX* is performing the first ultraviolet sky survey from space. It consists of a 50-cm UV–optimized modified Ritchey–Chrétien telescope, with a circular field-of-view (FOV) of $1^\circ 2'$ diameter. The *GALEX* instruments and mission are described fully in Martin et al. (2005) and Morrissey et al. (2005). Exposure times for NGC 2974 were 1477 s in both FUV (1350–1750 Å) and NUV (1750–2750 Å). Although the images are delivered pre-processed, we performed our own sky subtraction by measuring the sky level in source-free regions of the images. The spatial resolution of the images is approximately $4''.5$ and $6''.0$ FWHM in FUV and NUV, respectively, sampled with $1''.5 \times 1''.5$ pixels. We convolve the FUV data to the spatial resolution of the NUV observations to avoid spurious colour gradients in the inner parts.

We have performed surface photometry of NGC 2974 by measuring the surface brightness along elliptical annuli in the standard manner, using the ELLIPSE task within the STSDAS ISOPHOTE package in IRAF (Image Reduction and Analysis Facility). The centre of the isophotes was fixed to the centre of the light distribution and the position angle (PA), ellipticity (ϵ) and surface brightness (μ) were fitted as a function of radius, the latter increasing logarithmically to compensate for the rapid surface brightness decrease. The ellipses were fitted to the NUV image only, which has a far superior signal-to-noise ratio (S/N) at all radii, and were then imposed to the FUV image, so that meaningful colours can be derived. The fit fails at large radii due to low fluxes, so the position angle and ellipticity are kept fixed at those radii and only the surface brightness is measured. The necessary photometric zero-points were taken from Morrissey et al. (2005). Our UV surface brightness profiles extend to $2'$ (12.5 kpc for an assumed distance of 21.5 Mpc; Tonry et al. 2001) and reach depths of 29.0 and 28.6 AB mag arcsec $^{-2}$ in FUV and NUV, respectively. However, the nominal surface brightness limit for the 1477 s exposures used in our observations is roughly 28 AB mag arcsec $^{-2}$ in both bands (Martin et al. 2005). The difficulty of the sky subtraction is the main limiting factor.

2.2 Optical observations and data analysis

Ground-based optical imaging observations in the *HST* filter F555W (similar to Johnson *V*) were obtained with the MDM Observatory 1.3-m McGraw-Hill Telescope on 2003 March 26, again part of a larger survey targeting the whole SAURON galaxy sample. The MDM observations are described

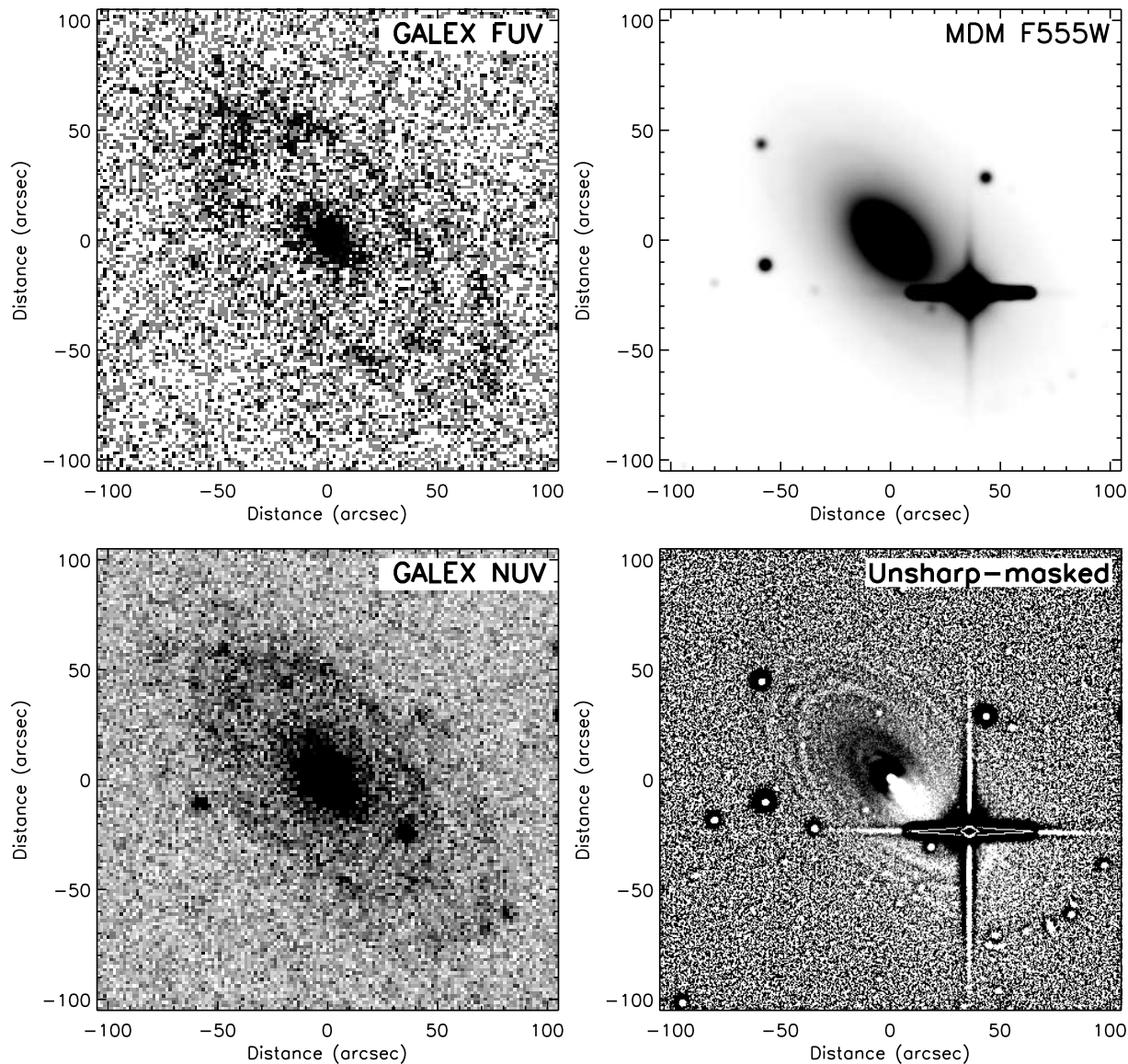


Figure 1. *GALEX* UV and MDM optical images of the central $100'' \times 100''$ of NGC 2974. *Top-left*: FUV image. *Bottom-left*: NUV image. *Top-right*: F555W image. *Bottom-right*: Unsharp-masked F555W image. Note the bright foreground star to the South-West.

in detail in Falc3n-Barroso et al. (2007, in prep.) and were reduced in the standard manner in IRAF. The FOV of the MDM images is $17'.3 \times 17'.3$ with $0''.508 \times 0''.508$ pixels, allowing for accurate sky subtraction and proper sampling of the seeing. The seeing for the NGC 2974 observations was $1''.2$, but the MDM data were also convolved to the resolution of the NUV data.

Surface photometry along ellipses was carried out for the MDM data in the same manner as for the *GALEX* data. The NUV ellipses were imposed on the MDM data and only the surface brightness was measured for each ellipse, allowing accurate UV–optical colours to be derived. An identical procedure was applied to *HST* WFPC2 images in the F555W filter, obtained from the Space Telescope European Coordinating Facility (ST-ECF) *HST* archive. The photometric zero-point of the MDM data was derived by scaling the MDM surface brightness profile to that of the *HST*

data, allowing for an arbitrary background level (the limited FOV of WFPC2 does not permit accurate sky subtraction). The MDM data necessary to photometrically calibrate the NGC 2974 imaging are available, but an *HST*-based calibration is both more accurate and more simple. Given the limited spatial resolution of *GALEX*, the *HST* data were used only to calibrate the MDM photometry. The MDM profiles extend to much greater radii than the *GALEX* profiles, but only the overlapping region is discussed here.

2.3 Results

Figure 1 shows the *GALEX* FUV, *GALEX* NUV, MDM F555W, and MDM F555W unsharp-masked images. The optical image has the smooth appearance characteristic of elliptical galaxies, but the UV images reveal at least two components. First, both FUV and NUV images show a

largely featureless central component with a rapidly decreasing surface brightness, which can probably be identified as a spheroid. Second, most distinct in the FUV, a complete ring is detected in the outer parts of the galaxy, at a radius of $\approx 60''$. The UV emission along this ring is patchy and it probably lies in a disc (see below). A partial ring is also suggested at a larger radius ($R \approx 90''$), wrapping over roughly 90° . Both rings are detected here for the first time and are primarily visible in the UV. However, a posteriori unsharp-masking of the MDM F555W image at full resolution does reveal hints of multiple narrow rings or tightly wound spirals arms at the right radii, more prominent in the North-East (see Fig. 1). Aperture photometry on the FUV image within the outer ring ($R \lesssim 60''$) yields a UV luminosity of $\approx 4.4 \times 10^8 L_\odot$. The luminosity in the outer ring itself ($50'' \lesssim R \lesssim 70''$) is $\approx 1.2 \times 10^8 L_\odot$.

Figure 2 shows the multi-colour surface photometry of NGC 2974 (all magnitudes are AB magnitudes; see also Table 1). In Figure 2a, the dashed line at $m_{\text{AB}} = 28 \text{ mag arcsec}^{-2}$ shows the nominal UV surface brightness limit for an exposure of 1477 s. The F555W and UV surface brightness profiles (Fig. 2a) show a relatively smooth decline with radius but also a small peak or plateau between 20 and $25''$. This peak may be associated with the large-scale bar postulated by Krajnović et al. (2005) and in Section 4. Indeed, Wozniak & Pierce (1991) found that the luminosity profiles of early-type barred galaxies all showed similar characteristic bumps, correlated with ellipticity peaks. Barred galaxies are also known to exhibit surface brightness plateaus (Freeman Type II profiles; e.g. Freeman 1970; MacArthur, Courteau & Holtzman 2003; Bureau et al. 2006). More strikingly, a broad secondary peak is clearly observed at $R \approx 60''$, particularly in the FUV, and can be identified with the outer ring. The partial ring at $R \approx 90''$ is also visible as a minor UV peak, but the S/N is very low. Figure 2g shows that, well inside the outer ring, the profile is roughly consistent with a de Vaucouleurs $R^{1/4}$ law (de Vaucouleurs 1958) in all bands. This is also the case at larger radii in the optical. The optical fit in Figure 2g is based on all data points with $R > 6''$, while the FUV and NUV fits are based on data with $6'' < R < 40''$ and $6'' < R < 35''$, respectively. The lower bound on the radius is necessary to avoid the bulk of the seeing effects.

Figure 3 shows that a population of age $\lesssim 0.5$ Gyr would exhibit $\text{FUV}-\text{NUV} \lesssim 1.0$, which is seen only in the central region ($R \lesssim 10''$) and near and beyond the newly-detected outer ring ($R \gtrsim 45''$). Studies of large samples of elliptical galaxies have indeed suggested that some have blue colours (e.g. Bertola, Burstein & Buson 1993) which can be explained by new generations of stars, and young stars are effectively traced by UV–optical colours. Using the empirical criteria of Yi et al. (2005) (based on NGC 4552 and M 32), thresholds below which we can reasonably expect the colours to indicate young stars (age $\lesssim 1$ Gyr) are shown as dashed lines in Figure 2b–d: $\text{FUV}-\text{NUV} = 1.0$, $\text{FUV}-\text{F555W} = 6.1$ and $\text{NUV}-\text{F555W} = 5.1$. Considering those UV–optical colours, it seems that young stellar populations are present in the core and around the outer ring, implying recent star formation in those two locations, despite the lack of other star formation evidence and the standard classification of NGC 2974 as an E4 elliptical. A note of caution is however necessary as strong FUV emission in the

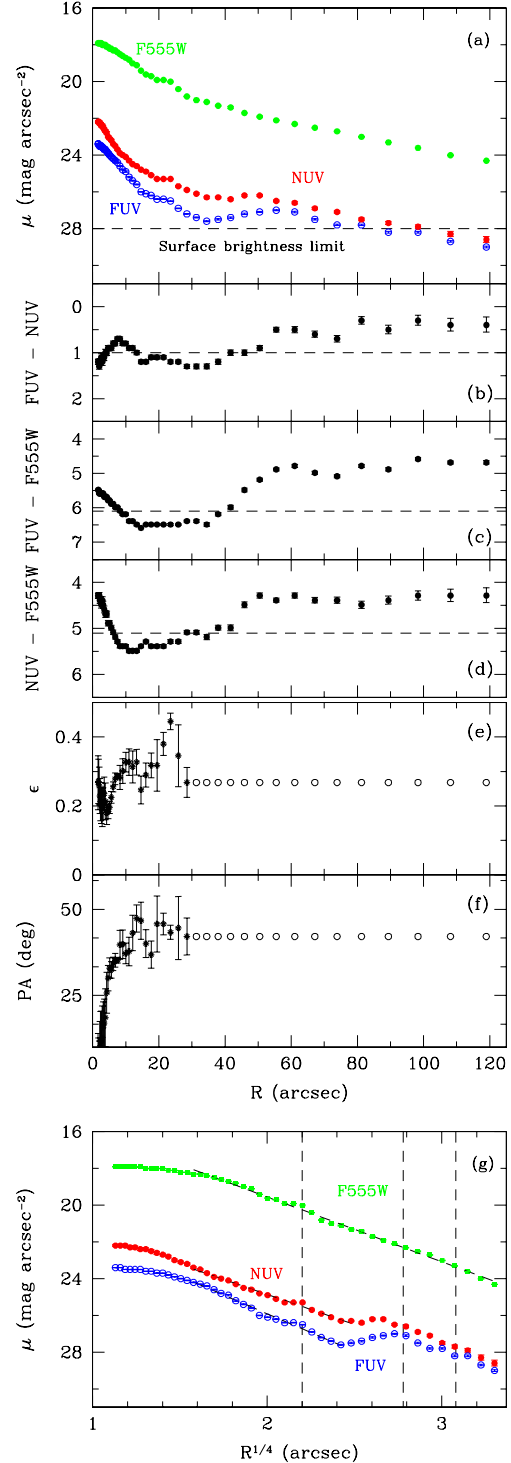


Figure 2. UV and optical surface photometry NGC 2974, from ellipse fitting. (a) F555W, NUV and FUV surface brightness profiles. The horizontal line shows the nominal UV surface brightness limit. (b)–(d) FUV–NUV, FUV–F555W and NUV–F555W colour profiles. (e)–(f) Ellipticity and position angle profiles derived from the NUV image. (g) F555W, NUV and FUV surface brightness profiles on a logarithmic radius scale. The features possibly associated with a large-scale bar ($R \approx 25''$), the outer ring ($R \approx 60''$) and the partial ring ($R \approx 90''$) are marked by vertical lines. $R^{1/4}$ fits are shown as straight lines (see text). Open circles in (e)–(f) indicate that the values were fixed, not fitted or measured.

Table 1. Radial profiles based on the ellipse fits

Radius ($''$)	μ_{FUV} (mag arcsec $^{-2}$)	μ_{NUV} (mag arcsec $^{-2}$)	μ_{F555W} (mag arcsec $^{-2}$)	$\log(t_{\text{YC}})$ (yr)	$\log(f_{\text{YC}})$	$\log(\Sigma_{\text{YC}})$ (M_{\odot} arcsec $^{-2}$)	$\log(\Sigma_{\text{VYC}})$ (M_{\odot} arcsec $^{-2}$)
1.64	23.39 ± 0.10	22.19 ± 0.09	17.91 ± 0.03	8.56 ^{+0.10} _{-0.10}	-2.10 ^{+0.40} _{-0.30}	6.15 ^{+0.06} _{-0.07}	6.15 ^{+0.06} _{-0.07}
1.80	23.43 ± 0.11	22.21 ± 0.11	17.92 ± 0.05	8.81 ^{+0.00} _{-0.05}	-2.10 ^{+0.18} _{-0.30}	6.12 ^{+0.06} _{-0.08}	6.12 ^{+0.06} _{-0.08}
1.98	23.51 ± 0.11	22.26 ± 0.11	17.92 ± 0.05	8.61 ^{+0.00} _{-0.15}	-2.00 ^{+0.00} _{-0.40}	6.09 ^{+0.07} _{-0.08}	6.09 ^{+0.07} _{-0.08}
2.18	23.52 ± 0.11	22.32 ± 0.12	17.93 ± 0.05	8.61 ^{+0.00} _{-0.15}	-2.00 ^{+0.00} _{-0.40}	6.05 ^{+0.07} _{-0.08}	6.05 ^{+0.07} _{-0.08}
2.39	23.54 ± 0.11	22.35 ± 0.12	17.95 ± 0.05	8.61 ^{+0.00} _{-0.15}	-2.00 ^{+0.00} _{-0.40}	5.99 ^{+0.07} _{-0.08}	5.99 ^{+0.07} _{-0.08}
2.63	23.57 ± 0.11	22.41 ± 0.12	17.97 ± 0.05	8.61 ^{+0.00} _{-0.15}	-2.05 ^{+0.05} _{-0.48}	5.93 ^{+0.08} _{-0.09}	5.93 ^{+0.08} _{-0.09}
2.90	23.64 ± 0.11	22.47 ± 0.13	18.01 ± 0.07	8.61 ^{+0.00} _{-0.15}	-2.05 ^{+0.05} _{-0.48}	5.87 ^{+0.08} _{-0.10}	5.87 ^{+0.08} _{-0.10}
3.18	23.69 ± 0.11	22.52 ± 0.13	18.03 ± 0.07	8.61 ^{+0.05} _{-0.15}	-2.10 ^{+0.10} _{-0.43}	5.81 ^{+0.09} _{-0.12}	5.81 ^{+0.09} _{-0.12}
3.50	23.72 ± 0.11	22.66 ± 0.13	18.05 ± 0.07	8.51 ^{+0.15} _{-0.30}	-2.40 ^{+0.40} _{-0.60}	5.74 ^{+0.11} _{-0.14}	5.74 ^{+0.11} _{-0.14}
3.86	23.77 ± 0.11	22.72 ± 0.12	18.07 ± 0.07	8.51 ^{+0.15} _{-0.30}	-2.40 ^{+0.40} _{-0.60}	5.63 ^{+0.12} _{-0.16}	5.63 ^{+0.12} _{-0.16}
4.23	23.84 ± 0.11	22.87 ± 0.11	18.12 ± 0.07	8.41 ^{+0.20} _{-0.35}	-2.70 ^{+0.60} _{-0.60}	5.48 ^{+0.11} _{-0.15}	5.48 ^{+0.11} _{-0.15}
4.65	23.92 ± 0.11	23.01 ± 0.11	18.16 ± 0.07	8.51 ^{+0.10} _{-0.09}	-2.42 ^{+0.30} _{-0.48}	5.41 ^{+0.11} _{-0.15}	5.41 ^{+0.11} _{-0.15}
5.13	24.08 ± 0.11	23.15 ± 0.10	18.21 ± 0.07	8.46 ^{+0.00} _{-0.90}	-2.70 ^{+1.48} _{-1.30}	5.13 ^{+0.11} _{-0.17}	5.13 ^{+0.11} _{-0.17}
5.64	24.14 ± 0.12	23.24 ± 0.10	18.25 ± 0.07	8.46 ^{+0.15} _{-0.90}	-2.70 ^{+0.40} _{-1.30}	5.21 ^{+0.11} _{-0.15}	5.21 ^{+0.11} _{-0.15}
6.20	24.23 ± 0.12	23.46 ± 0.10	18.31 ± 0.07	7.70 ^{+0.86} _{-0.11}	-4.00 ^{+1.48} _{-0.00}	5.05 ^{+0.11} _{-0.14}	5.05 ^{+0.11} _{-0.14}
6.83	24.36 ± 0.13	23.58 ± 0.09	18.37 ± 0.07	7.72 ^{+0.79} _{-0.09}	-4.00 ^{+1.30} _{-0.00}	4.89 ^{+0.11} _{-0.16}	4.89 ^{+0.11} _{-0.16}
7.50	24.47 ± 0.13	23.73 ± 0.09	18.43 ± 0.07	7.76 ^{+0.65} _{-0.08}	-4.00 ^{+1.00} _{-0.00}	4.77 ^{+0.12} _{-0.17}	4.77 ^{+0.12} _{-0.17}
8.25	24.62 ± 0.13	23.91 ± 0.08	18.55 ± 0.07	7.81 ^{+0.60} _{-0.11}	-4.00 ^{+1.00} _{-0.00}	4.41 ^{+0.09} _{-0.12}	4.41 ^{+0.09} _{-0.12}
9.08	24.84 ± 0.13	24.04 ± 0.08	18.62 ± 0.08	7.86 ^{+0.60} _{-0.12}	-4.00 ^{+1.00} _{-0.00}	4.36 ^{+0.07} _{-0.09}	4.36 ^{+0.07} _{-0.09}
9.99	24.95 ± 0.13	24.13 ± 0.08	18.71 ± 0.08	7.86 ^{+0.60} _{-0.12}	-4.00 ^{+1.00} _{-0.00}	4.65 ^{+0.08} _{-0.15}	4.65 ^{+0.08} _{-0.15}
10.98	25.25 ± 0.13	24.35 ± 0.08	18.83 ± 0.08	7.96 ^{+0.55} _{-0.01}	-4.00 ^{+1.00} _{-0.00}	4.54 ^{+0.06} _{-0.07}	4.54 ^{+0.06} _{-0.07}
12.08	25.46 ± 0.13	24.52 ± 0.08	19.02 ± 0.08	7.96 ^{+0.55} _{-0.14}	-4.00 ^{+1.00} _{-0.00}	4.77 ^{+0.07} _{-0.08}	4.77 ^{+0.06} _{-0.07}
13.29	25.67 ± 0.13	24.67 ± 0.08	19.17 ± 0.08	7.96 ^{+0.55} _{-0.01}	-4.00 ^{+1.00} _{-0.00}	4.84 ^{+0.06} _{-0.06}	4.77 ^{+0.06} _{-0.06}
14.61	26.04 ± 0.12	24.85 ± 0.08	19.42 ± 0.06	8.41 ^{+0.20} _{-0.55}	-3.30 ^{+0.78} _{-0.70}	4.79 ^{+0.05} _{-0.05}	4.61 ^{+0.05} _{-0.05}
16.08	26.13 ± 0.12	24.99 ± 0.08	19.65 ± 0.06	8.36 ^{+0.25} _{-0.55}	-3.30 ^{+0.78} _{-0.70}	4.86 ^{+0.05} _{-0.06}	4.58 ^{+0.05} _{-0.06}
17.69	26.25 ± 0.12	25.12 ± 0.09	19.78 ± 0.06	8.36 ^{+0.25} _{-0.55}	-3.30 ^{+0.78} _{-0.70}	4.80 ^{+0.05} _{-0.06}	4.57 ^{+0.05} _{-0.06}
19.46	26.42 ± 0.12	25.32 ± 0.09	19.91 ± 0.06	8.36 ^{+0.25} _{-0.55}	-3.30 ^{+0.60} _{-0.70}	4.75 ^{+0.05} _{-0.05}	4.47 ^{+0.05} _{-0.05}
21.41	26.49 ± 0.12	25.33 ± 0.08	19.94 ± 0.06	8.36 ^{+0.30} _{-0.50}	-3.52 ^{+1.00} _{-0.48}	4.85 ^{+0.04} _{-0.04}	4.61 ^{+0.04} _{-0.04}
23.54	26.53 ± 0.12	25.35 ± 0.09	20.02 ± 0.09	8.36 ^{+0.30} _{-0.50}	-3.30 ^{+0.78} _{-0.70}	4.77 ^{+0.04} _{-0.05}	4.56 ^{+0.04} _{-0.05}
25.89	26.91 ± 0.12	25.71 ± 0.09	20.45 ± 0.07	8.46 ^{+0.20} _{-0.55}	-3.00 ^{+0.60} _{-1.00}	4.85 ^{+0.04} _{-0.05}	4.27 ^{+0.04} _{-0.05}
28.49	27.25 ± 0.13	25.93 ± 0.09	20.88 ± 0.07	8.51 ^{+0.20} _{-0.30}	-2.70 ^{+0.60} _{-0.70}	4.84 ^{+0.04} _{-0.04}	3.77 ^{+0.04} _{-0.04}
31.34	27.46 ± 0.13	26.17 ± 0.09	21.06 ± 0.08	8.61 ^{+0.05} _{-0.35}	-2.52 ^{+0.22} _{-0.78}	4.88 ^{+0.04} _{-0.05}	3.87 ^{+0.04} _{-0.04}
34.46	27.63 ± 0.13	26.32 ± 0.10	21.14 ± 0.10	8.56 ^{+0.10} _{-0.70}	-2.70 ^{+0.40} _{-1.30}	4.90 ^{+0.04} _{-0.04}	3.48 ^{+0.04} _{-0.04}
37.91	27.54 ± 0.13	26.36 ± 0.09	21.38 ± 0.09	8.56 ^{+0.10} _{-0.40}	-2.52 ^{+0.37} _{-0.78}	4.70 ^{+0.04} _{-0.04}	3.84 ^{+0.04} _{-0.04}
41.70	27.41 ± 0.14	26.41 ± 0.10	21.43 ± 0.10	8.46 ^{+0.15} _{-0.87}	-2.70 ^{+0.40} _{-1.30}	4.72 ^{+0.04} _{-0.05}	3.86 ^{+0.04} _{-0.05}
45.87	27.23 ± 0.14	26.23 ± 0.10	21.79 ± 0.10	8.56 ^{+0.05} _{-0.40}	-2.15 ^{+0.39} _{-0.85}	4.65 ^{+0.04} _{-0.04}	4.09 ^{+0.04} _{-0.04}
50.46	27.18 ± 0.13	26.24 ± 0.10	21.94 ± 0.09	8.56 ^{+0.05} _{-0.30}	-2.05 ^{+0.05} _{-0.65}	4.73 ^{+0.04} _{-0.04}	4.26 ^{+0.04} _{-0.04}
55.50	27.02 ± 0.13	26.53 ± 0.09	22.12 ± 0.08	7.86 ^{+0.65} _{-0.64}	-3.30 ^{+1.15} _{-0.70}	4.50 ^{+0.03} _{-0.04}	4.30 ^{+0.03} _{-0.04}
61.05	27.12 ± 0.14	26.67 ± 0.10	22.35 ± 0.08	8.06 ^{+0.45} _{-0.88}	-3.00 ^{+0.90} _{-1.00}	4.47 ^{+0.04} _{-0.04}	4.14 ^{+0.04} _{-0.04}
67.16	27.53 ± 0.14	26.92 ± 0.11	22.52 ± 0.08	8.26 ^{+0.30} _{-1.01}	-2.70 ^{+0.65} _{-1.30}	4.56 ^{+0.04} _{-0.04}	3.92 ^{+0.04} _{-0.04}
73.88	27.89 ± 0.14	27.14 ± 0.12	22.78 ± 0.08	8.46 ^{+0.10} _{-0.60}	-2.30 ^{+1.00} _{-0.30}	4.50 ^{+0.05} _{-0.05}	3.29 ^{+0.05} _{-0.05}
81.26	27.85 ± 0.14	27.56 ± 0.13	23.05 ± 0.08	7.30 ^{+0.06} _{-0.08}	-4.00 ^{+1.48} _{-0.00}	3.82 ^{+0.06} _{-0.07}	3.37 ^{+0.06} _{-0.07}
89.39	28.23 ± 0.15	27.78 ± 0.14	23.32 ± 0.08	7.86 ^{+0.60} _{-0.62}	-3.30 ^{+1.00} _{-0.70}	3.41 ^{+0.09} _{-0.11}	2.60 ^{+0.09} _{-0.11}
98.33	28.26 ± 0.14	27.91 ± 0.15	23.65 ± 0.06	8.00 ^{+0.45} _{-0.87}	-3.00 ^{+0.78} _{-1.00}	2.41 ^{+0.13} _{-0.19}	1.83 ^{+0.13} _{-0.19}
108.15	28.71 ± 0.14	28.33 ± 0.19	24.04 ± 0.06	7.81 ^{+0.65} _{-0.65}	-3.30 ^{+1.08} _{-0.70}	—	—
118.98	29.02 ± 0.15	28.61 ± 0.22	24.32 ± 0.06	7.81 ^{+0.65} _{-0.65}	-3.30 ^{+1.08} _{-0.70}	—	—

Columns: (1) Major-axis radius; (2)–(4) surface brightnesses in the FUV, NUV and F555W filters; (5)–(6) age and mass fraction of the young component; (7) surface mass densities of the young component from the pixel-by-pixel analysis shown in Figure 8; (8) same as (7) but including only the very young stars (age < 0.5 Gyr).

central parts does not always indicate RSF. The FUV–NUV and FUV–F555W colours in these regions are close to those of typical UV upturn galaxies (e.g. NGC 1399, Bica et al. 1996; NGC 4552, Ferguson et al. 1991), where old helium-burning stars are believed to be the primary FUV sources. The UV bright outer ring is however difficult to explain with

He-burning stars, as the UV upturn phenomenon is generally found in galaxy cores.

The morphology of NGC 2974 is also revealing (Fig. 2e–h). The NUV ellipticity is somewhat noisy outside of the central region ($R \gtrsim 10''$) but is consistent with a single value $\epsilon \approx 0.35$. The ellipticity drops continuously at smaller radii,

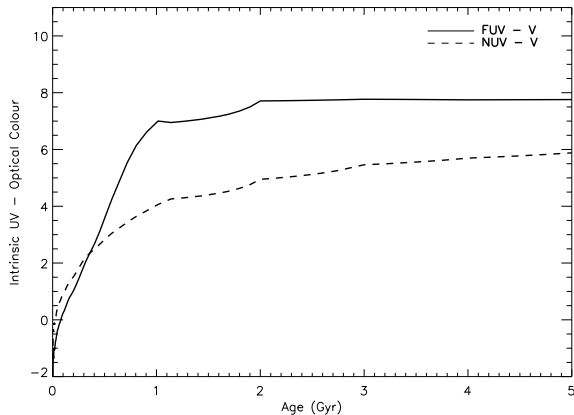


Figure 3. UV–optical colours of single stellar populations as a function of age (see Yi 2003). Solid and dashed lines show, respectively, the FUV–V and NUV–V colour. The evolution in UV–optical colours slows down dramatically after 1 Gyr.

reaching $\epsilon \approx 0.15$ in the centre. This suggests that the two components seen in the FUV and NUV images have different flattening, the inner component being rounder (i.e. spheroid-like) and the outer component flatter (i.e. disc-like). Some evidence in fact suggest that NGC 2974 has a stellar disc, although it is probably quite thick (e.g. Krajnović et al. 2005). While invalid for this thick disc and the stellar spheroid traced, e.g., by the optical light, the thin disc approximation is probably acceptable for the UV light tracing (very) young stars (see Section 3), at the very least in the outer ring, since those stars were presumably born in a thin gaseous disc. For an infinitely thin disc, $\epsilon = 0.35$ implies an inclination $i = 49^\circ$, somewhat smaller than the values of $55\text{--}65^\circ$ derived by previous studies (e.g. Kim et al. 1988; Amico et al. 1993; Buson et al. 1993; Cinzano & van der Marel 1994; Plana et al. 1998; Krajnović et al. 2005). However, ellipse fitting fails at large radii. Measuring the axial ratio of the outer ring directly on the FUV image yields an ellipticity $\epsilon = 0.43$, corresponding to an inclination of 55° , in better agreement with previous works. It is thus likely that the newly-identified UV rings lie in a relatively thin disc in the equatorial plane of NGC 2974.

The NUV position angle is also noisy but roughly constant outside the central region. At $R \lesssim 10''$, however, the position angle varies continuously. This isophotal twist suggests an asymmetry in the central region, consistent with the presence of a nuclear bar or nuclear spiral arms, although it could equally be due to dust (e.g. Emsellem et al. 2003). The NUV Fourier coefficients a_3 and a_4 , which measure deviations of the isophotes from a pure ellipse (e.g. Lauer 1985; Bender & Möllenhoff 1987; Jędrzejewski 1987), are essentially consistent with zero at all radii (not shown).

3 STELLAR POPULATIONS AND STAR FORMATION

3.1 Distribution of young and old stars

Baade (1944) proposed the existence of two kinds of stellar populations by analyzing the colours and brightnesses of

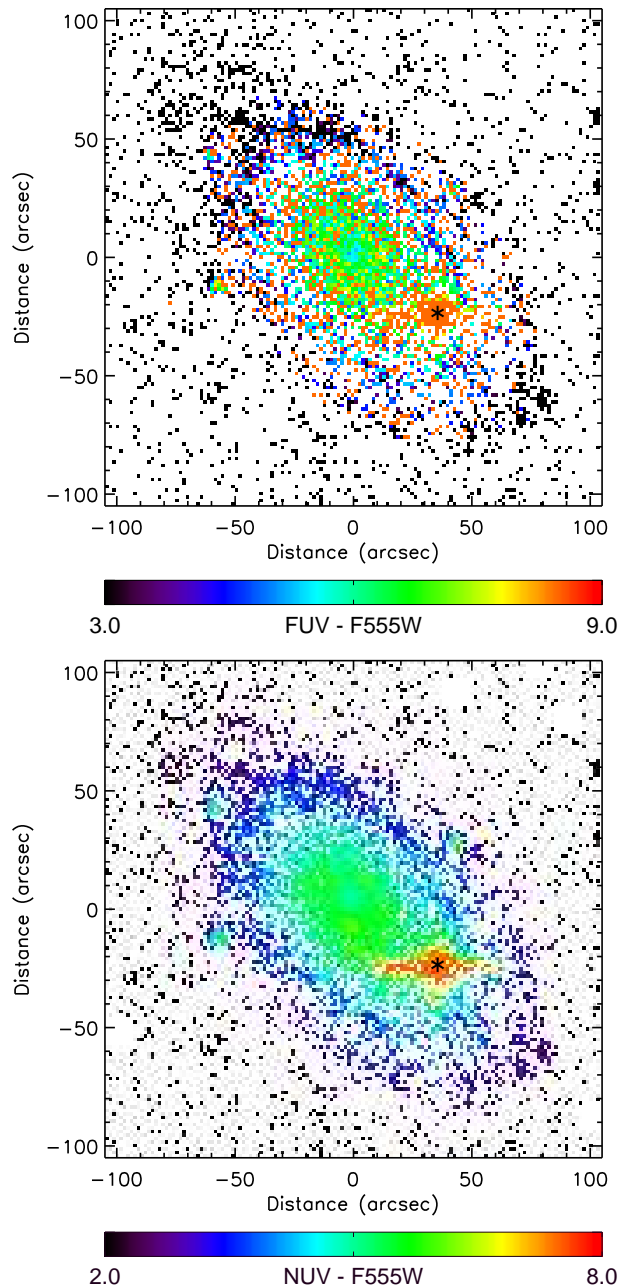


Figure 4. UV–optical colour maps of NGC 2974. *Top:* FUV–F555W. *Bottom:* NUV–F555W. A star marks the area contaminated by the foreground star.

nearby spiral and elliptical galaxies: population I, containing highly luminous O and B type stars; and population II, containing luminous red stars. He also suggested that elliptical galaxies consist of population II stars in a gas and dust-free environment. In the past sixty years, however, many surveys have detected (extended) gaseous discs in ellipticals, and atomic (e.g. Kim et al. 1988; Weijmans et al. 2006), ionised (e.g. Bettoni 1992; Demoulin-Ulrich, Butcher & Bokserberg 1984; Kim 1989; Goudfrooij et al. 1994; Plana et al. 1998) and X-ray (e.g. Forman, Jones & Tucker 1985) gas have all been detected in NGC 2974. Detailed studies of the colours and brightnesses of stars revealed that the distinction be-

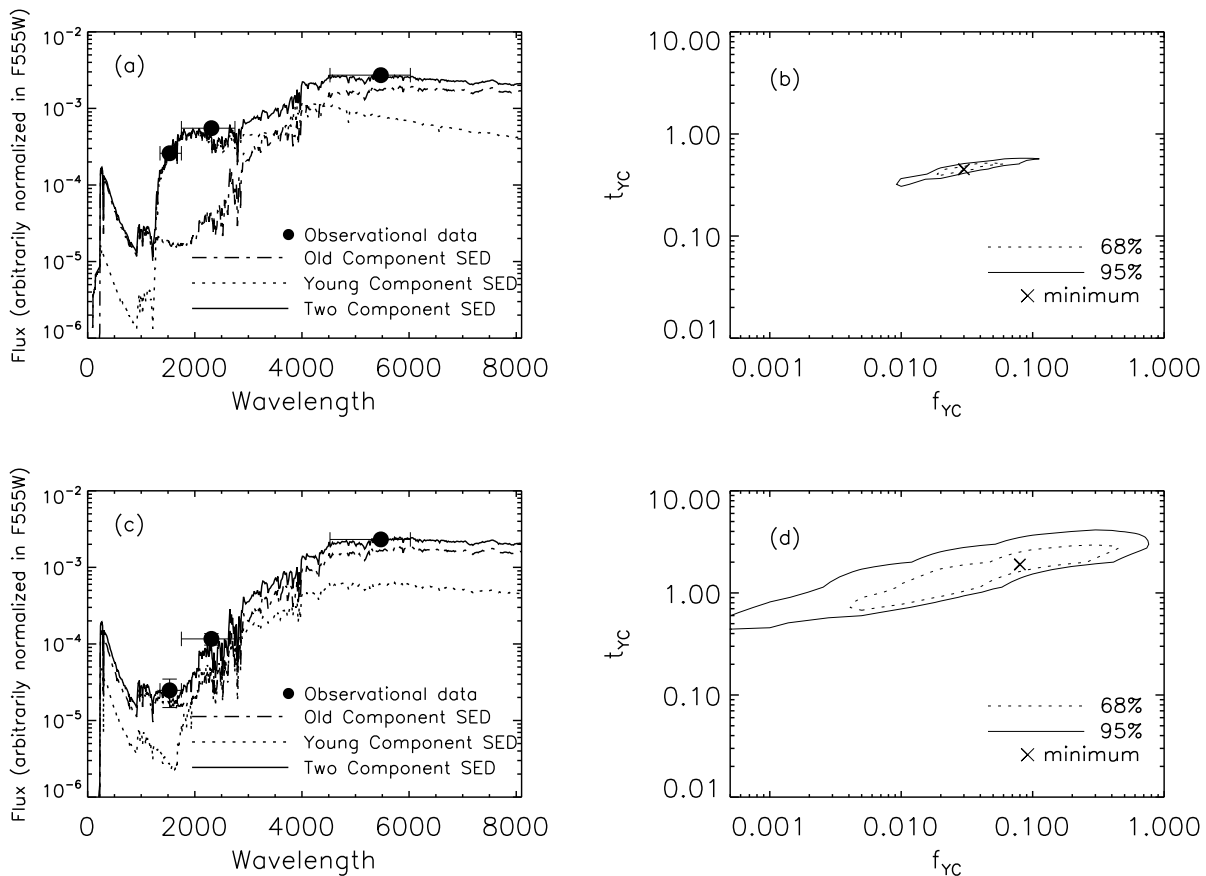


Figure 5. Examples of two-component stellar population fits. (a) Model spectra, where the dotted and dot-dashed spectra represent the young and old component, respectively, while the solid spectrum is the sum. (b) χ^2 contours, where the best fit is marked with an ‘x’. The dotted and dot-dashed contours represent the 68 and 95 per cent confidence levels, respectively. This example from the outer ring has a non-negligible fraction (≈ 3 per cent) of very young (0.45 Gyr) stars. (c)–(d) Same as (a)–(b) but for an example at intermediate radius ($R \approx 35''$), where the age and mass fraction of the young component are poorly constrained.

tween populations I and II is also one of age. Some elliptical galaxies (including NGC 2974) have blue UV colours, and this is believed to be caused mainly by young stars (see Section 2.3).

Most UV photons are emitted by stars younger than $\sim 10^9$ yr, so the UV luminosity is closely related to the RSF history of the galaxy. While radial profiles such as those shown in Figure 2 are very useful, they do not allow to study the detailed spatial distribution of young stars, and so we have constructed full two-dimensional UV–optical colour maps, shown in Figure 4. The FUV–NUV colour map is very noisy, and thus in the following analysis we restrict ourselves to pixels with $S/N > 2$ in both FUV and NUV.

The FUV–F555W colour map clearly shows the blue colour ($FUV-F555W \lesssim 6.1$) of the outer ring and outskirts of NGC 2974, suggesting that young stars are an important contributor to the galaxy’s UV luminosity. With $FUV-F555W \approx 5.5$, the central regions also likely harbour young stars, while the intermediate regions are red ($FUV-F555W \gtrsim 6.1$). Those trends are fully supported by the NUV–F555W colours, where $NUV-F555W \lesssim 5.1$ traces young stars. It also appears that there are more young stars

in the North-East half of the outer ring than to the South-West.

3.2 Age and mass fraction of young stars

In order to estimate the age, mass fraction and surface mass density of the young stellar component, we consider a two-stage star formation history, whereby stars are formed instantaneously at two different times. The first starburst is fixed at high redshift (12 Gyr) and represents an old stellar component. It is based on a metallicity-composite population (a short burst with chemical enrichment) with a mean metallicity of roughly solar, which includes the UV upturn phenomenon originating from old hot HB stars (see Kodama & Arimoto 1997). The second burst has a fixed metallicity (solar) but its age and relative magnitude are left to vary. The free parameters of the model are thus the age (t_{YC}) and stellar mass fraction (f_{YC}) of the young stellar component, and we explore a wide range of values for both: $10^{-3} \leq t_{YC} \leq 10$ Gyr and $10^{-6} \leq f_{YC} \leq 1$. The surface mass density of the young component (Σ_{YC}) is then calculated by simply multiplying f_{YC} by the total surface

mass density, obtained here directly from the F555W surface brightness assuming a purely old population, a reasonable approximation given the small values of f_{YC} derived everywhere.

The models of Yi (2003), updated to allow a wider choice of initial mass functions (Yi & Yoon, in prep.), are used. Since those models do not cover ages younger than 1 Gyr, we combine them with the models of Bruzual & Charlot (2003) at an age of 1 Gyr. The connection between the two sets of models is reasonably smooth, as illustrated in Figure 3 which shows the intrinsic UV–V colours of a simple stellar population (SSP) as a function of age. Clearly, small values of UV–optical colours trace young stars. Furthermore, the UV emission in star-forming galaxies is dominated by short-lived stars (e.g. Kennicutt 1998), so the evolution of the UV–optical colours slows down dramatically after 1 Gyr.

To determine the age and the mass fraction of the young component, we fit the observed UV and optical colours (FUV–F555W and NUV–F555W) to those returned by the two-component model. Dust extinction is expected to be small everywhere in NGC 2974, so for simplicity we do not correct for it. The mass fraction of the young component is then formally a lower limit, since dust would mainly affect the FUV and NUV filters. For illustration, Figure 5 shows the fit and χ^2 contours (68 per cent and 95 per cent confidence levels) for two different locations (pixels) in the galaxy. The dotted and dot-dashed spectra represent the young and old component, respectively, while the solid spectrum is the sum. In the first case, taken in the outer ring, there is strong evidence for a stellar component younger than 0.5 Gyr. In the second, taken at intermediate radius ($R = 35''$), the age and mass fraction of the young component are poorly constrained. The shape of the χ^2 contours illustrates the usual age-mass degeneracy, whereby a small amount of very young stars has a similar effect to a larger amount of older stars.

In Figure 6, we show the best estimates of (t_{YC} , f_{YC} , Σ_{YC}) using two-dimensional maps. Pixels with $\chi^2 > 1.5$ (bad fits) are shown in white, as are fits with a negligible young component. The age map clearly shows very young stars (< 500 Myr) in both the central regions and in and around the newly-identified UV rings, as suggested by the FUV data (e.g. Fig. 1). The prominence of the central spheroid compared to the outer ring in both UV images can probably be explained by the fact that, while the mass fraction in the young component is not particularly high in the centre, the total surface mass density there is approximately 50 times higher than in the outer ring (e.g. Fig. 2), resulting in a much higher absolute surface mass density for the young component. Interestingly, there is also a sprinkling of young stars at intermediate radii, between the inner spheroid and the outer ring, and there are comparatively more (very) young stars to the North-East edge of the outer ring than to the South-West. There is however considerable pixel-to-pixel scatter. The mass fraction map clearly shows that the fractional contribution of the young component is rather low in the centre but increases outward, explaining the very blue colours of NGC 2974 near the outer ring.

To reduce the scatter and highlight radial trends better, we also applied our two-component model to the radial profiles shown in Figure 2, where the radial bins have much higher S/N than individual pixels. The resulting radial pro-

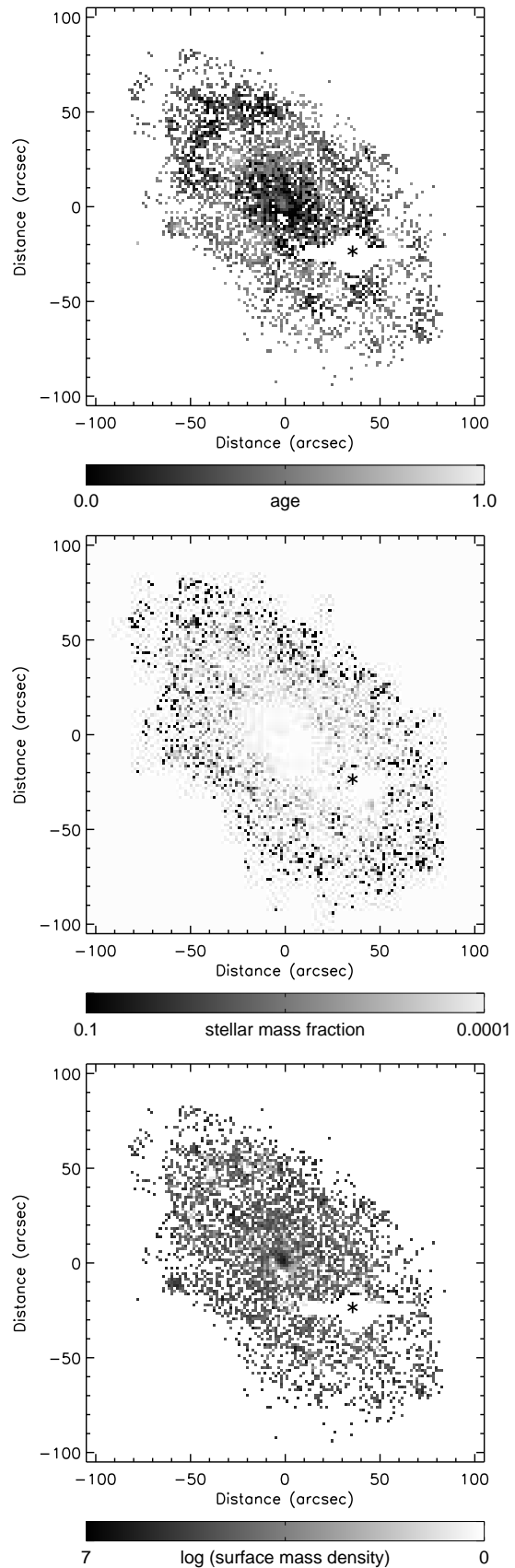


Figure 6. Two-component fit maps for the pixels with $S/N > 2$. Age (*top*) in unit of Gyr, stellar mass fraction (*middle*) and surface mass density in unit of $M_{\odot} \text{ arcsec}^{-2}$ (*bottom*) of the young stellar component. A star marks the area contaminated by the foreground star.

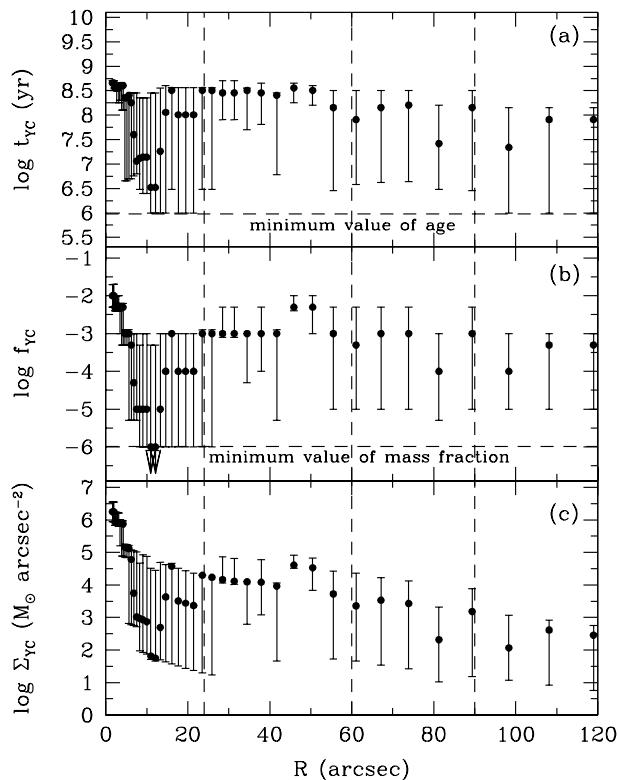


Figure 7. Two-component fit radial profiles. Errors show the ranges of the fitting model parameters that are within 1σ confidence from the best-fit model. Age (a), stellar mass fraction (b) and surface mass density (c) of the young stellar component. The vertical lines show the radial positions of the large-scale bar ($R \approx 25''$), the outer ring ($R \approx 60''$) and the partial ring ($R \approx 90''$), respectively.

files of the age, stellar mass fraction and surface mass density of the young component are shown in Figure 7. Errors show the ranges of the fitting model parameters that are within 1σ confidence from the best-fit model. These clearly show a young stellar component with age 0.1–0.4 Gyr in the inner $10''$ and around the outer ring. The presence of young stars (age 0.2–0.4 Gyr) is also confirmed at intermediate radii ($10'' \lesssim R \lesssim 40''$). This may seem somewhat odd considering the FUV map in Figure 1, but it is in agreement with the NUV map. The mass fraction profile in Figure 7 clearly shows that the stellar mass fraction in the young component is below 1 per cent everywhere. Interestingly, the youngest stars are found just inside $10''$ (although their mass fraction is very small), where the [O III] equivalent width map reveals a nuclear ring (see Section 4.1). Such rings are usually associated with star formation, although the $H\beta/[O III]$ line ratio in that case is more characteristic of shocks or low ionization nuclear emission regions (LINERS; see, e.g., Sarzi et al. 2006).

The errors bars in Figure 7 are driven primarily by the inability of the stellar population models to properly fit the data (see Fig. 5), rather than by the uncertainty in the data themselves. To reduce the scatter in Figure 7, we have thus azimuthally averaged the pixel-by-pixel analysis shown in Figure 6 along the same ellipses. The resulting radial profiles of the surface mass densities in the young component and

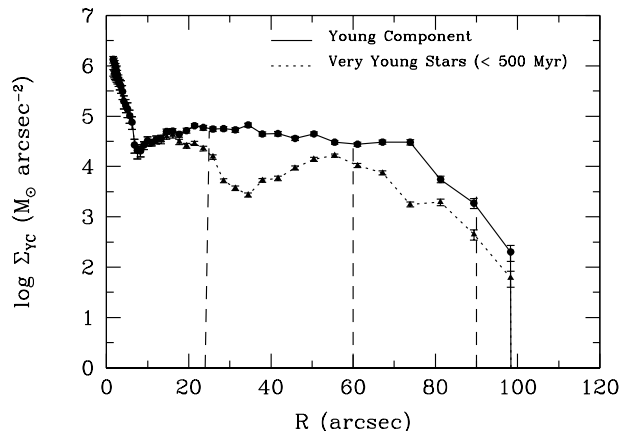


Figure 8. Radial profiles of the surface mass density in the young stellar component, for two different age cuts. While Figure 7c is based on the radial profiles from ellipse fitting shown in Figure 2, this figure is based on azimuthal averages of the pixel-by-pixel analysis of Figure 6. The errors are the standard deviation of the mass fractions derived for individual pixels and should not be compared to those in Figure 7c. The vertical lines show the radial positions of the large-scale bar ($R \approx 25''$), the outer ring ($R \approx 60''$) and the partial ring ($R \approx 90''$), respectively.

in “very young” stars (< 500 Myr) are shown in Figure 8 (see also Table 1). The very young stars clearly reproduce the preponderance of the central regions and outer ring. The total stellar mass implied by the luminosity of NGC 2974 is about $1.2 \times 10^{11} M_{\odot}$, but the total mass in the young component is only roughly $7.9 \times 10^8 M_{\odot}$ or 0.66 per cent of the total stellar mass.

The young component dominates the total UV flux of this galaxy but has a minor (< 10 per cent) effect in the optical ($\approx 5000 \text{ \AA}$). For example, the outer and partial rings are hardly detected at V band (see Fig.1). Hence, optical age estimates on this (e.g. Denicoló et al. 2005; Kuntschner et al. 2007, in prep.) or any other galaxies with minor RSF would not be influenced much.

All our modeling results slightly depend on the choice of the input parameters for the two-component modeling. For instance, if we assume 14 Gyr for the age of the old component instead of 12 Gyr, the total mass fraction of the young component becomes slightly less, 0.6 per cent. No difference is seen for an old component of 10 Gyr. This is because at large ages, old populations develop hot HB stars (UV upturn phenomenon). Since the UV upturn is thought to be prominent only for large ages, the degeneracy between the UV upturn and the RSF is negligible for younger ages, i.e. 8–12 Gyr. The choice of metallicity for the young component has no significant effect on the derived parameters.

4 FIGURE ROTATION

4.1 Resonance rings

Rings such as those observed in the UV in NGC 2974 are often seen in disc galaxies, where they can generally be explained by the so-called resonance ring formation, relating the shapes and positions of the rings to the presence of resonances in the discs (e.g. Schwarz 1981, 1984a; Byrd et al.

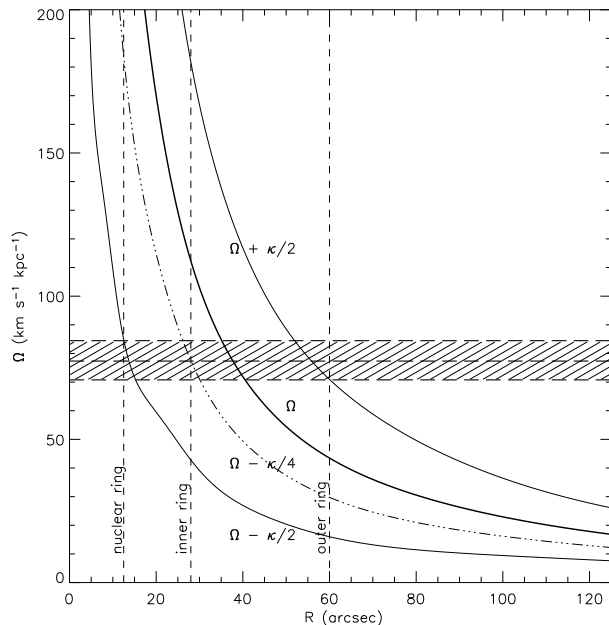


Figure 9. Resonance diagram for NGC 2974. Profiles of Ω (thick solid line), $\Omega \pm \kappa/2$ (thin solid lines) and $\Omega - \kappa/4$ (dot-dashed line) are shown. Vertical dashed lines show the positions of the *GALEX* and *SAURON* rings, while thick horizontal dashed lines show the implied pattern speeds.

1994). Given a circular velocity curve and the presence of an $m = 2$ perturbation such as a bar, the pattern speed fixes the existence and position of resonances and thus the orbit families present in the disc (see, e.g., Sellwood & Wilkinson 1993).

Krajnović et al. (2005) constructed a detailed mass model of NGC 2974 from optical observations, in order to reproduce its stellar and gas kinematics within the radial range probed by their *SAURON* observations. The mass model nevertheless extends farther and allows to predict the circular velocity curve (and epicyclic frequency) to the larger radii probed by *GALEX*, where the rotation curve is currently unknown (but see Kim et al. 1988; Zeilinger et al. 1996; Weijmans et al. 2006). Figure 9 shows the rotation and other frequencies ($\Omega \pm \kappa/2$, $\Omega - \kappa/4$) predicted from this model, as well as the location of the major rings observed in the *GALEX* UV and *SAURON* ionised-gas data.

As discussed in Section 2.3, the UV ring detected in the *GALEX* data has a radius of $60''$. Placing this on the frequencies diagram, and assuming that this ring traces the outer Lindblad resonance (OLR; i.e. that the ring is an outer ring), we obtain a pattern speed of about $72 \text{ km s}^{-1} \text{ kpc}^{-1}$ (at the intersection with the $\Omega + \kappa/2$ curve).

Although not as clear as the *GALEX* UV ring, the [O III] equivalent width map of Krajnović et al. (2005; see also Sarzi et al. 2006), adapted in Figure 10, suggests a (pseudo-)ring near the edge of the *SAURON* FOV, at a radius of roughly $28''$. Placing this ring on the frequencies diagram, and assuming that it traces corotation (i.e. that it is an inner ring), we obtain a pattern speed of roughly $112 \text{ km s}^{-1} \text{ kpc}^{-1}$ (at the intersection with the Ω curve). This is inconsistent with the value obtained from the *GALEX* outer ring, even allowing for a large uncertainty in the radius. However, assuming

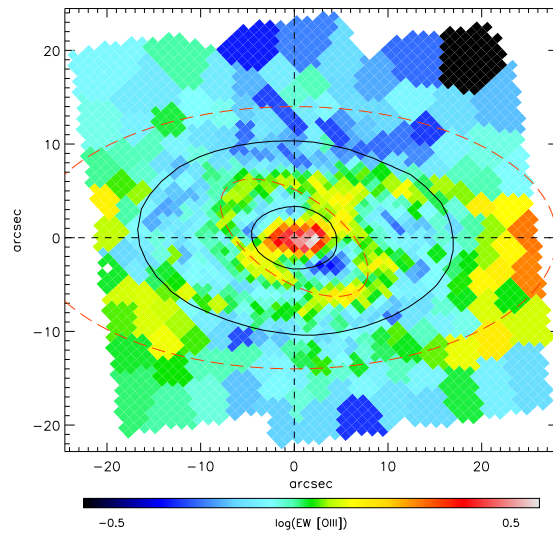


Figure 10. Equivalent width map of the [O III] emission line as observed by *SAURON* (adapted from Krajnović et al. 2005). Overplotted are two isophotes from the reconstructed broadband image (solid lines) and the outlines of the nuclear and inner rings discussed in Section 4.1 (dashed lines). The image has been rotated so that the galaxy major-axis lies horizontal.

instead that this inner ring is located at the inner ultra harmonic resonance (IUHR), as is argued equally often (e.g. Schwarz 1984b; Buta 1995; Patsis et al. 2003), we obtain a pattern speed of roughly $77 \text{ km s}^{-1} \text{ kpc}^{-1}$ (at the intersection with the $\Omega - \kappa/4$ curve), in good agreement with the value from the *GALEX* outer ring.

The *SAURON* [O III] equivalent width map further reveals a much smaller ring, with a radius of $9''$ along its major-axis. This ring is clearly misaligned from the main body of the galaxy, however, and assuming a galaxy inclination of 59° (the value preferred by Krajnović et al. 2005) and an orientation relative to the galaxy major-axis of 34° , its deprojected radius is $13''$. Placing this on the frequencies diagram, and assuming that this innermost ring traces the inner Lindblad resonance (ILR; i.e. that it is a nuclear ring), we obtain a pattern speed of about $84 \text{ km s}^{-1} \text{ kpc}^{-1}$ (at the intersection with the $\Omega - \kappa/2$ curve). This value is slightly higher than that obtained from the *GALEX* outer ring and the *SAURON* [O III] inner ring, but it is consistent given the steepness of the $\Omega - \kappa/2$ curve in the inner regions and the uncertainty on the ring’s radius (an increase of only $1\text{--}2''$ in the deprojected ring radius brings the pattern speeds in agreement).

4.2 Pattern speed

Given the above results, we argue that NGC 2974 has a non-negligible asymmetry and harbours a large-scale $m = 2$ pattern, most likely a large-scale bar, with a pattern speed of $78 \pm 6 \text{ km s}^{-1} \text{ kpc}^{-1}$. The small surface brightness plateau observed at radii $20\text{--}25''$ (see Section 2.3) suggests a bar length of $\approx 23''$ (end of the plateau), just consistent with Krajnović et al. (2005) who suggest a large-scale bar radius

Table 2. Pattern speeds of lenticular galaxies

Galaxy	Type	Pattern speed (km s ⁻¹ kpc ⁻¹)	Reference
NGC 936	SB(rs)0 ⁺	104	1
NGC 936	SB(rs)0 ⁺	60 ± 14	2
NGC 1023	SB(rs)0 ⁻	104 ± 34	3
NGC 1308	SB(r)0/a	99.4 ± 34.8	4
NGC 1358	SAB(r)0/a	31 ± 15	5
NGC 1440	(L)SB(rs)0 ⁺	83.0 ± 19.1	4
NGC 2950	(R)SB(r)0 ⁰	99.2 ± 21.2	6
NGC 3412	SB(s)0 ⁰	56.7 ± 15.5	4
NGC 4596	SB(r)0 ⁺	52 ± 13	7
IC 874	SB(rs)0 ⁰	41.6 ± 14.3	4
ESO 139-G009	(RL)SB(rl)0 ⁰	61.4 ± 16.6	4
ESO 281-G031	SB(rl)0 ⁰	27 ± 11	5
NGC 7079	(L)SB(r)0 ⁰	45.5 ± 1.1	8

References: (1) Kent (1987); (2) Merrifield & Kuijken (1995); (3) Debattista et al. (2002); (4) Aguerrri et al. (2003); (5) Gerssen et al. (2003); (6) Corsini et al. (2003); (7) Gerssen et al. (1999); (8) Debattista & Williams (2004).

of 12.5–25". The bar would then fit nicely inside the [O III] inner ring (radius 28") but would end well inside its own corotation radius (see Fig. 9), with a corotation to bar radius ratio of about 1.6, slightly higher than expected and typically observed in barred disc galaxies (1.2 for fast bars; see, e.g., Athanassoula 1992; Aguerrri, Debattista & Corsini 2003; Gerssen, Kuijken & Merrifield 2003). Krajnović et al. (2005) do suggest a pattern speed of 185 km s⁻¹ kpc⁻¹, significantly different from ours, but we are confident in our estimate as higher values do not allow any major resonance at the large radius where the *GALEX* ring is found (see Fig. 9). For a pattern speed of 185 km s⁻¹ kpc⁻¹ and a bar radius of 23", the bar would then also extend beyond its own corotation radius (see Fig. 9), a situation forbidden on orbital grounds (e.g. Contopoulos 1980).

Table 2 presents a compilation of all direct bar pattern speed measurements in lenticular galaxies, all of them obtained with the method of Tremaine & Weinberg (1984) or variations of it (e.g. Merrifield & Kuijken 1995). As can be seen from Table 2, all measured values lie in the range 25–105 km s⁻¹ kpc⁻¹. A value of 78 ± 6 km s⁻¹ kpc⁻¹ thus appears normal, while 185 km s⁻¹ kpc⁻¹ would be exceptional.

We also note that the pattern speed of Krajnović et al. (2005) was obtained by combining the relatively simple gas model of Emsellem et al. (2003), yielding the pattern speed of the nuclear bar detected, with the assumption that the corotation of the nuclear bar coincides with the ILR of the large-scale bar (see Fig. 7 of Krajnović et al. 2005). However, if the pattern speed of the nuclear bar is accurate, the arguments above suggest instead that it is the OLR of the nuclear bar (rather than its corotation) which coincides with the ILR of the large-scale bar, consistent with the apparent elongation of the nuclear ring perpendicular to the nuclear bar (see Fig. 10). Of course, all of the above arguments assume linear perturbations and localised resonances, so perfect matches should not be expected, and many possibilities exist for nuclear bar–large-scale bar (non-linear) coupling (e.g. Friedli & Martinet 1993; Masset & Tagger 1997).

In the [O III] equivalent width map, the nuclear (radius

13") and inner (radius 28") rings appear connected by two arc-like structures reminiscent of spiral arms. The H α + [N II] map of Emsellem et al. (2003) reveals smaller spiral arms within the nuclear ring, but the two spiral systems appear to wind in opposite directions. Based on the central dust distribution (more prominent to the East; e.g. Sarzi et al. 2006) and the ionised gas and stellar kinematics (North-East half receding; e.g. Emsellem et al. 2004), it is clear that the nuclear spiral (within the nuclear ring) is trailing while the larger-scale spiral (between the nuclear and inner rings) is leading. To our knowledge, this is the first time this configuration is observed, but it is unclear how to generate such a system within the framework of linear perturbation theory. The reverse combination of a leading nuclear spiral and trailing larger-scale spiral can be generated by a potential with a large-scale bar and constant density core (producing an inner ILR; see, e.g., Wada 1994, 2001; Maciejewski 2004), but this is ruled out by Krajnović et al.'s (2005) mass model and Figure 9 (the potential is cuspy to the smallest observable scales). We have thus as yet no proper explanation for this behaviour, but it may well offer a way to better understand the coupling between nuclear and large-scale bars.

4.3 Star formation – dynamics connection

Weijmans et al. (2006; see also Weijmans et al. 2007, in prep.) have obtained new HI synthesis observations of NGC 2974, which reveal that the HI is confined to a very regular although lopsided (i.e. more HI to the North-East) broad ring, extending from roughly $R = 50''$ to $120''$. These observations naturally solve the issue of the fuel for the RSF detected here. The newly-identified UV outer ring at $60''$ is located at the inner edge of the HI ring, while the incomplete UV ring at larger radii is closer to the outer edge of the HI. Furthermore, the HI lopsidedness to the North-east matches very well the extra RSF detected there.

Interestingly, while the UV (which is primarily sensitive to young stars up to ≈ 1 Gyr) does detect a young population, optical studies (which are primarily sensitive to slightly older stellar populations; e.g. Denicoló et al. 2005; Kuntschner et al. 2007, in prep.) have not provided any evidence for young stars. This suggests either that bursts of star formation previous to the ones detected here were too small to be detected optically, or that this is the first burst in a long time. Although the morphology and kinematics of the HI ring detected by Weijmans et al. are very regular, the lower spatial resolution observations of Kim et al. (1988) do reveal a more irregular structure, with a small extension to the South-East. It is thus possible that the HI was only recently accreted.

It is unclear whether the ionised gas detected in the inner parts in the optical (e.g. Fig. 10) originates in the HI. Bar torques are such that gas normally flows from corotation to the OLR, not the other way around. This can explain why the HI has accumulated in the ring observed by Weijmans et al., but makes it difficult for any gas to trickle down the center. Whether the ionised gas has the same origin as the HI thus presumably depends on exactly how the HI was accreted.

5 SUMMARY

We have presented *GALEX* FUV and NUV and ground-based F555W imaging of the nearby early-type galaxy NGC 2974. The optical images are characteristic of elliptical galaxies but the UV images reveal both a central spheroid-like component and a complete (outer) ring of radius 6.2 kpc. Another partial ring is also suggested at an even larger radius. Both rings are detected here for the first time and are only visible in the UV. The FUV luminosity of the outer ring is $\approx 1.2 \times 10^8 L_{\odot}$.

Blue FUV–NUV colours are observed in the centre of the galaxy and around the outer ring, suggesting the presence of young stellar populations ($\lesssim 1$ Gyr) and recent star formation. UV–optical colours are also blue at both locations, indicating that (very) young stars contribute significantly to the galaxy’s UV flux. Simple two-component stellar population modeling allows us to constrain the age, stellar mass fraction and surface mass density of the young component pixel by pixel and confirms this behaviour. The latter are formally lower limits since we have not corrected for dust extinction, but the effect is expected to be small.

Considering the mass model and observations of Krajnović et al. (2005), the SAURON [O III] nuclear and inner rings and the *GALEX* UV outer ring are all consistent with a single pattern speed of $78 \pm 6 \text{ km s}^{-1} \text{ kpc}^{-1}$, suggesting that NGC 2974 harbours a large-scale $m = 2$ asymmetry such as a bar. Assuming that the surface brightness plateau observed at a radius of 20–25'' marks its limits, this large-scale bar would end at roughly 60 per cent of its own corotation radius, slightly smaller but not inconsistent with expectations.

Star formation, rings and bars are not topics normally associated with elliptical galaxies, yet in recent years we have seen a growing number of studies reporting evidence for complex kinematics (e.g. Emsellem et al. 2004) and recent star formation (e.g. Yi et al. 2005). The origin of those features are of key importance. Here, we have witnessed evidence for recent star formation in a particular early-type galaxy, in the form of a ring, fueled by a newly discovered co-spatial ring of neutral hydrogen (Weijmans et al. 2006). A rotating bar (i.e. a disc phenomenon) seems to be regulating both phenomena, adding to earlier evidence for lenticular-like properties in NGC 2974. Star formation may thus not be all that unusual in early-type galaxies, or perhaps elliptical galaxies in the classical sense are simply far rarer than usually assumed.

ACKNOWLEDGMENTS

The authors thank the referee, S. Trager, for numerous comments which led to improvement in the paper. We would like to thank S. Kaviraj and K. Schawinski for useful discussions, and T. de Zeeuw, E. Emsellem, H. Kuntschner, R. Peletier and M. Sarzi for comments on the manuscript. HJ acknowledges support from the International Research Internship Program of the Korea Science and Engineering Foundation. MB acknowledges support from NASA through *GALEX* Guest Investigator program GALEXGI04-0000-0109. This work was supported by grant No. R01-2006-000-10716-0 from the Basic Research Program of the

Korea Science and Engineering Foundation to SKY. RLD is grateful for the award of a PPARC Senior Fellowship (PPA/Y/S/1999/00854) and postdoctoral support through PPARC grant PPA/G/S/2000/00729. The PPARC Visitors grant (PPA/V/S/2002/00553) to Oxford also supported this work. Based on observations made with the NASA Galaxy Evolution Explorer. *GALEX* is operated for NASA by the California Institute of Technology under NASA contract NAS5-98034. Photometric data were also obtained using the 1.3m McGraw-Hill Telescope of the MDM Observatory. Part of this work is based on data obtained from the ESO/ST-ECF Science Archive Facility. This project made use of the HyperLeda and NED databases.

REFERENCES

- Aguerri J. A. L., Debattista V. P., Corsini E. M., 2003, *MNRAS*, 338, 465
- Amico P., et al., 1993, in Danziger I. J., Zellinger W. W., Kjaerp K., eds, *Structure, Dynamics and Chemical Evolution of Elliptical Galaxies*. ESO, Garching, p. 225
- Athanassoula E., 1992, *MNRAS*, 259, 345
- Baade W., 1944, *ApJ*, 100, 137
- Bacon R., et al., 2001, *MNRAS*, 326, 23
- Bender R., Möllenhoff C., 1987, *A&A*, 177, 71
- Bertola F., Burstein D., Buson L. M., 1993, *ApJ*, 403, 573
- Bettoni D., 1992, *A&AS*, 96, 333
- Bica E., Alloin D., 1987, *A&AS*, 70, 281
- Bica E., Bonatto C., Pastoriza M. G., Alloin D., 1996, *A&A*, 313, 405
- Bruzual G., Charlot S., 2003, *MNRAS*, 344, 1000
- Bureau M, Aronica G., Athanassoula E., Dettmar R.-J., Bosma A., Freeman K. C., 2006, *MNRAS*, in press
- Burgarella D., Buat V., Iglesias-Páramo J., 2005, *MNRAS*, 360, 1413
- Buson L. M., et al., 1993, *A&A*, 280, 409
- Buta R., 1995, *ApJS*, 96, 39
- Byrd G., Rautiainen P., Salo H., Buta R., Crocker D. A., 1994, *AJ*, 108, 476
- Cinzano P., van der Marel R. P., 1994, *MNRAS*, 270, 325
- Code A. D., Welch G. A., Page T., 1972, in A. D. Code, ed, *Scientific Results from the Orbiting Astronomical Observatory (OAO-2)*. NASA SP-310, p. 559
- Contopoulos G., 1980, *A&A*, 81, 198
- Corsini E. M., Debattista V. P., Aguerri J. A. L., 2003, *ApJ*, 599, L29
- Debattista V. P., Corsini E. M., Aguerri J. A. L., 2002, *MNRAS*, 332, 65
- Debattista V. P., Williams T. B., 2004, *ApJ*, 605, 714
- Demoulin-Ulrich M.-H., Butcher H. R., Boksenberg A., 1984, *ApJ*, 285, 527
- Denicoló G., Terlevich R., Terlevich E., Forbes D. A., Terlevich A., 2005, *MNRAS*, 358, 813
- de Vaucouleurs G., 1958, *ApJ*, 128, 465
- de Vaucouleurs G., de Vaucouleurs A., Corwin H. G. Jr, Buta R. J., Paturel H. G., Fouqué P., 1991, 3rd Reference Catalogue of Bright Galaxies, Springer-Verlag, New York (RC3)
- de Zeeuw P. T., et al., 2002, *MNRAS*, 329, 513
- de Zeeuw P. T., Franx M., 1991, *ARA&A*, 29, 239
- Dressler A., Gunn J. E., 1983, *ApJ*, 270, 7

- Eggen O. J., Lynden-Bell D., Sandage A. R., 1962, *ApJ*, 136, 748
 Emsellem E., Goudfrooij P., Ferruit P., 2003, *MNRAS*, 345, 1297
 Emsellem E., et al., 2004, *MNRAS*, 352, 721
 Ferguson H. C., et al., 1991, *ApJL*, 382, 69
 Ferreras I., Silk J., 2000, *ApJL*, 541, L37
 Forman W., Jones C., Tucker W., 1985, *ApJ*, 293, 102
 Freeman K. C., 1970, *ApJ*, 160, 811
 Friedli D., Martinet L., 1993, *A&A*, 277, 27
 Fukugita M., Nakamura O., Turner E. L., Helmboldt J., Nichol R. C., 2004, *ApJL*, 601, L127
 Gerssen J., Kuijken K., Merrifield M. R., 1999, *MNRAS*, 306, 926
 Gerssen J., Kuijken K., Merrifield M. R., 2003, *MNRAS*, 345, 261
 Gott J. R., 1977, *ARA&A*, 15, 235
 Goudfrooij P., Hansen L., Jorgensen H. E., Norgaard-Nielsen H. U., 1994, *A&AS*, 105, 341
 Hau G. K. T., Carter D., Balcells M., 1999, *MNRAS*, 306, 437
 Hirashita H., Buat V., Inoue A. K., 2003, *A&A*, 410, 83
 Hunter D. A., Gillett F. C., Gallagher J. S., Rice W. L., Low F. J., 1986, *ApJ*, 303, 171
 Jedrzejewski R. I., 1987, *MNRAS*, 226, 747
 Kennicutt R. C., 1983, *ApJ*, 272, 54
 Kennicutt R. C., 1998, *ARA&A*, 36, 189
 Kent S. M., 1987, *AJ*, 93, 1062
 Kim D.-W., 1989, *ApJ*, 346, 653
 Kim D.-W., Jura M., Guhathakurta P., Knapp G. R., van Gorkom J. H., 1988, *ApJ*, 330, 684
 Kodama T., Arimoto N., 1997, *A&A*, 320, 41
 Krajnović D., Cappellari M., Emsellem E., McDermid R. M., de Zeeuw P. T., 2005, *MNRAS*, 357, 1113
 Kuntschner H., et al., 2006, *MNRAS*, 369, 497
 Larson R. B., 1974, *MNRAS*, 166, 385
 Lauer T. R., 1985, *MNRAS*, 216, 429
 MacArthur L. A., Courteau S., Holtzman J. A., 2003, *ApJ*, 582, 689
 Maciejewski W., 2004, *MNRAS*, 354, 883
 Martin D. C., et al., 2005, *ApJ*, 619, L1
 Masset F., Tagger M., 1997, *A&A*, 322, 442
 Merrifield M. R., Kuijken K., 1995, *MNRAS*, 274, 933
 Meurer G. R., Gerhardt R., Heckman T. M., Lehnert M. D., Leitherer C., Lowenthal J., 1997, *AJ*, 114, 54
 Morrissey P., et al., 2005, *ApJ*, 619, L7
 O'Connell R. W., 1980, *ApJ*, 236, 430
 O'Connell R. W., 1999, *ARA&A*, 37, 603
 Patsis P. A., Skokos Ch., Athanassoula E., 2003, *MNRAS*, 346, 1031
 Peletier R. F., Davies R. L., Illingworth G. D., Davies L. E., Cawson M., 1990, *AJ*, 100, 1091
 Plana H., Boulesteix J., Amram P., Carignan C., Mendes de Oliveira C., 1998, *A&AS*, 128, 75
 Raimann D., Storchi-Bergmann T., Quintana H., Hunstead R., Wisotzki L., 2005, *MNRAS*, 364, 1239
 Sarzi M., et al., 2006, *MNRAS*, 366, 1151
 Schwarz M. P., 1981, *ApJ*, 247, 77
 Schwarz M. P., 1984a, *MNRAS*, 209, 93
 Schwarz M. P., 1984b, *PASA*, 5, 464
 Schweizer F., Seitzer P., 1992, *AJ*, 104, 1039
 Sellwood J. A., Wilkinson A., 1993, *Re. Prog. Phys.*, 56, 173
 Tonry J. L., Dressler A., Blakeslee J. P., Ajhar E. A., Fletcher A. B., Luppino G. A., Metzger M. R., Moore C. B., 2001, *ApJ*, 546, 681
 Trager S. C., Faber S. M., Worthey G., Gonzalez J. J., 2000, *AJ*, 119, 1645
 Tremaine S., Weinberg M. D., 1984, *ApJL*, 282, L5
 Wada K., 1994, *PASJ*, 46, 165
 Wada K., 2001, *PASJ*, 53, 1163
 Weijmans A., Krajnovic D., Oosterloo T. A., Morganti R., de Zeeuw P. T., 2006, in J. Palous, F. Combes, eds., *Galaxy Evolution across the Hubble Time*. Cambridge University Press), p. 406
 Wozniak H., Pierce M. J., 1991, *A&AS*, 88, 325
 Yi S. K., 2003, *ApJ*, 582, 202
 Yi S., Demarque P., Oemler A. J., 1997, *ApJ*, 486, 201
 Yi S. K., et al., 2005, *ApJL*, 619, L111
 Zeilinger W. W., et al., 1996, *A&AS*, 120, 257